

Research



Cite this article: Shemesh M, Addadi L, Geiger B. 2017 Surface microtopography modulates sealing zone development in osteoclasts cultured on bone. *J. R. Soc. Interface* **14**: 20160958. <http://dx.doi.org/10.1098/rsif.2016.0958>

Received: 29 November 2016
Accepted: 25 January 2017

Subject Category:

Life Sciences—Chemistry interface

Subject Areas:

biomaterials

Keywords:

bone roughness, actin dynamics, atomic force microscopy

Author for correspondence:Benjamin Geiger
e-mail: benny.geiger@weizmann.ac.il

Electronic supplementary material is available online at <https://dx.doi.org/10.6084/m9.figshare.c.3685576>.

Surface microtopography modulates sealing zone development in osteoclasts cultured on bone

Michal Shemesh^{1,2}, Lia Addadi¹ and Benjamin Geiger²

¹Department of Structural Biology, Weizmann Institute of Science, 7610001 Rehovot, Israel

²Department of Molecular Cell Biology, Weizmann Institute of Science, Wolfson Building for Biological Research, Room 618, 234 Herzl Street, 7610001 Rehovot, Israel

MS, 0000-0002-0782-5991

Bone homeostasis is continuously regulated by the coordinated action of bone-resorbing osteoclasts and bone-forming osteoblasts. Imbalance between these two cell populations leads to pathological bone diseases such as osteoporosis and osteopetrosis. Osteoclast functionality relies on the formation of sealing zone (SZ) rings that define the resorption lacuna. It is commonly assumed that the structure and dynamic properties of the SZ depend on the physical and chemical properties of the substrate. Considering the unique complex structure of native bone, elucidation of the relevant parameters affecting SZ formation and stability is challenging. In this study, we examined in detail the dynamic response of the SZ to the microtopography of devitalized bone surfaces, taken from the same area in cattle femur. We show that there is a significant enrichment in large and stable SZs (diameter larger than 14 μm ; lifespan of hours) in cells cultured on rough bone surfaces, compared with small and fast turning over SZ rings (diameter below 7 μm ; lifespan approx. 7 min) formed on smooth bone surfaces. Based on these results, we propose that the surface roughness of the physiologically relevant substrate of osteoclasts, namely bone, affects primarily the local stability of growing SZs.

1. Introduction

Bone is composed mainly of type I collagen, mineralized by carbonated hydroxyapatite crystals and assembled in a complex hierarchical structure [1]. Bone is continuously remodelled by the coordinated action of two cell types: osteoclasts, which resorb old or damaged bone, and osteoblasts, which deposit new bone [2–4]. Tight, multi-level regulation of the bone remodelling process is enabled by cross-coordinated action of these two cell types, as well as bone-embedded osteocytes [5,6]. This process is regulated by diverse signalling systems, including the receptor activator of nuclear factor kappa-B ligand (RANKL) pathway [7,8].

Osteoclast resorption depends on its tight adhesion to the bone surface [9], which is mediated via an actin-rich integrin adhesion structure known as the sealing zone (SZ). SZ formation and turnover are highly sensitive to the local environment, including surface chemistry [10–12], adhesiveness [13,14] and its physical properties, such as microtopography [15,16].

The SZ is a belt-like structure, consisting of a condensed array of podosomes, the basic adhesion structures of osteoclasts and other monocytic cells (e.g. macrophages and dendritic cells) [17]. Podosomes, in turn, contain a central actin core, about 200 nm in diameter, oriented perpendicularly to the plasma membrane and several micrometres high [10]. The actin core of individual podosomes is surrounded by a peripheral adhesion ring, 0.5–1 μm in diameter, containing integrins and associated plaque proteins that mediate the adhesion to the bone surface [18–23]. The unique structure of podosomes, combined with their rapid turnover [18,24] and assembly into coherent SZ

rings, suggest that they play a key role in sensing the surface and regulating bone resorption.

Indeed, previous studies indicated that osteoclasts seeded on different surfaces, both natural and artificial, display distinct SZ organizations and dynamic properties [25]. Especially intriguing is the apparent confinement of SZ to specific regions on bone, which differs from the rather uniform distribution of SZ on surfaces such as calcite or glass. Owing to the complexity and heterogeneity of native bone surfaces, the mechanism underlying this spatial selectivity of SZ stabilization remains unclear.

Among the diverse parameters that were considered as potential local stimulators of SZ formation on bone, we chose to focus here on the effect of surface microtopography. In general, it was established that differences in the topography of adhesive surfaces can exert major effects on cell spreading [26], motility [27,28] and the formation of matrix adhesions [29,30]. In the context of bone remodelling, previous studies described the effect of surface topography on osteoclast differentiation [16], resorption activity [31] and SZ dimensions and dynamics [32]. In particular, the three-dimensional SZ architecture tends to adapt to the surface geometry [33], and ring translocation is arrested by local topographic barriers [15]. Topography sensing can also have physiological relevance, given the presence of structures in bone that induce local remodelling, such as micro-cracks [34,35]; bones that show extensive cracking have rougher fractured surfaces [36] (RMS in humans = $310 \pm 44 \mu\text{m}$ [34]). In addition, topography was shown to be an important factor in bone substitutions and osseointegration, as rough implant–bone interfaces promote extensive bone remodelling shortly after implantation and promote the re-establishment of normal remodelling activity by increasing the interfacial shear strength [37].

That being said, the inherent difficulty in accurately defining local variations of surface roughness and the related chemical properties of natural surfaces result in difficulty to assess the direct mechanism whereby microtopography affects osteoclast adhesion on the physiologically relevant substrate, namely, bone.

To address this issue, we plated RAW 264.7 murine osteoclast precursors, both non-expressing and stably expressing actin labelled with green fluorescent protein (GFP-actin), on devitalized bone surfaces displaying distinct microtopographies and examined, using different imaging approaches, the effects of surface roughness on the structure and dynamics of the SZ. The microtopography of the bone surfaces was directly measured using non-destructive atomic force microscopy (AFM) imaging in liquid. Live-cell fluorescence imaging of osteoclasts growing on rough and smooth bone surfaces showed a multi-level response: small and short lived SZs developed with adhesion time into stable, growing SZs. This development is more pronounced on rough surfaces, where enhanced bone microtopography contributes to the local stabilization of the growing rings.

2. Material and methods

2.1. Preparation of bone surfaces

Longitudinal bone slices, with an area of $5 \times 5 \text{ mm}$ and a thickness of 1 mm were retrieved from young cattle femurs, obtained 1 day post-mortem from a local butcher shop (Moo&Moo,

Rehovot, Israel). To prepare slices, the bone was cut using a low-speed diamond saw (South Bay Technology, Inc.), in the mid area between the anterior and posterior sides, at a location displaying osteonal arrangement of the mineralized collagen bundles, and with defined longitudinal directionality. To avoid drying damage, the bone was kept hydrated throughout the entire experiment. For comparison of bone topography, we took two slices from neighbouring positions. One of the slices was then further polished (in a Minimet 1000 grinder-polisher, BUEHLER, Chicago, IL, USA) using abrasive paper (MicroCut Discs, P1200, P1500, P2500 grit; BUEHLER, Chicago, IL, USA). The polishing parameters were kept constant throughout all experiments (8 min at speed 15 for paper P1200; 15 min at speed 10 for paper P1500; and additional 15 min at speed 10 for paper P2500). The force for all polishing papers was kept at 1 N. To avoid chemical modification of the bone surface, no diamond paste was used. The polished bone surfaces were carefully rinsed several times using a jet of double distilled water and examined under an optical microscope to ensure complete removal of particles.

2.2. Atomic force microscopy characterization and roughness analysis

Polished and unpolished bone slices were scanned using an atomic force microscope (NanoWizard³ Bioscience, JPK Instruments, Berlin, Germany), as described in [38]. Images were taken using contact mode in liquid (cell culture media, see §2.3). Pyramidal silicon nitride triangular cantilevers (DNP) with a nominal stiffness of 0.12 N m^{-1} and a nominal radius of 20 nm were used (Bruker Corporation, Camarillo, CA, USA). Imaging parameters (SetPoint = 1 V; line rate = 0.7 Hz; IGain = 100 Hz) were kept constant for all samples, to enable accurate comparison between the different surfaces [39]. Scans of both 10 and 100 μm areas were taken from different bone slices, each at seven different locations. The surface topography does not vary significantly from site to site, with standard error one order of magnitude smaller than the roughness value. The height images, corrected for tilt distortion [40] were calculated using the WsXM software [41].

To describe the dependence of surface roughness at the measurement scale, we applied power spectral density (PSD) analysis to the 100 μm AFM height scans, using WsXM software, and derived the relevant roughness from the volume underneath the PSD function [42] (for details, see electronic supplementary material).

2.3. Tissue culture, cell differentiation and bone plating

RAW 264.7 cells, both not expressing, as well as stably expressing GFP-actin [24] were obtained from the American Type Culture Collection (ATCC; Manassas, VA, USA), cultured in Dulbecco's modified Eagle medium (DMEM) with Earle's salts, supplemented with 1% L-glutamine and NaHCO_3 , 10% fetal bovine serum (FBS; Gibco, Grand Island, NY, USA) and antibiotics (1% pen-strep; Biological Industries, Beit Haemek, Israel). For osteoclast differentiation, RAW cells were seeded on plastic dishes ($100 \text{ cells mm}^{-2}$) in alpha MEM with Earle's salts, L-glutamine and NaHCO_3 (Sigma, Rehovot, Israel), and supplemented with FBS and antibiotics, 20 ng ml^{-1} recombinant soluble receptor activator of NF κ B ligand (RANKL), and 20 ng ml^{-1} macrophage colony-stimulating factor (R&D Systems Minneapolis, MN, USA) at 37°C in a 5% CO_2 humidified atmosphere for 60 h. Differentiation medium was changed every 24 h. Once differentiated (indicated by cell morphology), cultures were treated with 10 mM EDTA for 10 min, and the cells were centrifuged, resuspended in differentiation medium, and replated on the bone surface. Prior to cell plating, bone surfaces were

coated with vitronectin ($10 \mu\text{g ml}^{-1}$) for 10 h at 4°C , to increase the amount of adhering cells (after ensuring that this treatment has no influence on the cell area and SZ size and dynamic properties) then washed three times with culture medium, and heated to 37°C .

2.4. Fluorescence microscopy

For live-cell imaging, RAW 264.7 osteoclasts expressing GFP-actin were used. The differentiated cells were replated on bone slices, and allowed to adhere for 24 h. The slices were then imaged upside-down on a MatTek glass-bottomed dish (#P35G-0-20-C, MatTek Corp., Ashland, MA, USA). Time-lapse images were acquired with an automated inverted microscope (DeltaVision Elite system IX71 equipped with auto-focus system and a Resolve3D software modulus; Applied Precision, Inc., GE Healthcare, Issaquah, WA, USA) using $20\times/0.85$ or $40\times/1.30$ oil objectives (Olympus, Tokyo, Japan). The microscope is equipped with an environmental box kept at 37°C , in a 5% CO_2 humidified atmosphere. Images were acquired every 1 min for about 20 h. For fixed-sample imaging, cells were simultaneously permeabilized with 0.5% Triton X-100 (Fluka-Chemie AG, Switzerland), and fixed in warm 3% paraformaldehyde (Merck, Darmstadt, Germany). Then, specimens were washed three times with phosphate-buffered saline, and stained for actin (FITC-phalloidin, Sigma) and nuclei (Hoechst 33342, Life Technologies, Thermo Fisher Scientific Corp., Carlsbad, CA, USA). Temporal ratio images were produced as previously described [43]. Briefly, the pixel intensity values of frames ' $t + 1$ ' were divided by the intensity values of the corresponding pixel at time ' t ', producing a spectral image in which blue indicates loss of actin intensity, red indicates newly formed actin-rich structures and yellow indicates stable actin fluorescence.

2.5. Statistical analysis

Data on fixed samples were acquired for populations of 1268 SZ rings on smooth bone surfaces, and 1061 SZ rings on rough bone surfaces. For the live experiments, a total of 104/75 SZ rings on rough and smooth bone surfaces, respectively, were tracked, and the number of frames in which they were visible as a superstructure, calculated as their lifetime. Out of the total SZs counted, populations of 57/54 small SZ rings, fusion events for 13/12 SZ rings, and expansion for 7/7 SZ rings on rough/smooth topographies, respectively, were analysed. Shape descriptors for individual hand-marked rings were extracted using Fiji (analyse-measure), as well as an intensity plot against line distance (analyse-plot profile) [44]. Statistical significance (Student's t -test) was determined using data analysis in EXCEL. The quality of linear fit to the individual kinetic plots in figure 5 was determined according to a residual plot showing the lack of trend, sufficiently small significance F , and the upper and lower confidence intervals. Box charts were generated using Origin Pro8 software (OriginLab Corporation, Northampton, MA, USA). Synchronization between the kinetics of different ring pairs was determined by cross correlation [45].

3. Results

3.1. The cortical bone surfaces show complex topography

Bone surfaces were prepared as described and imaged with wet mode AFM. Bone specimens were kept wet at all times, to avoid structural modifications due to dehydration [46]. The surface topography of both rough and smooth bone slices displayed complex patterns, depending on the scale of measurement (figure 1). Representative scan areas of

$100 \mu\text{m}$ of the unpolished, rough bone surface (figure 1*a,c*), show very different topographies compared with those of the polished, smooth bone (figure 1*b,c*). On the rough surface, the saw markings constitute the dominant feature, creating periodic ridges and gorges about $20 \mu\text{m}$ wide, with height differences (peak-to-valley) of around $1 \mu\text{m}$ (boxed area in figure 1*c*). By contrast, the smooth, polished bone surface (figure 1*b,c*) displays a lower and more uniform topography, with peak-to-valley differences of the order of 200 nm . Both topographies at this scale (tens of μm) show irregular surfaces with multiple small peaks superimposed on the larger peaks. Focusing to an area of $10 \mu\text{m}$ increases the AFM imaging resolution and enables better detection of the lower level topography (figure 1*d-f*). The smaller features, few μm wide, show height differences of $100\text{--}200 \text{ nm}$ on both bone topographies (figure 1*f*). Zooming further to show scan area of $2.5 \mu\text{m}$ (figure 1*g,h*) and height profile of $1 \mu\text{m}$ (figure 1*i*) shows small protrusions, 200 nm wide, and several tens of nm high on both topographies.

Overall, this surface characterization indicates that the bone surfaces we have created contain multiple topographic signals at different lateral scales. Such complex topography requires a suitable analysis of bone roughness, capable of separating the contributions of bone surface features with different lateral dimensions to the complex topography observed. For this purpose, PSD analysis is a useful method for the decomposition of surface roughness into features that appear at different characteristic relevant sizes, i.e. at different wavelengths [42] (for further details, see §2.2). PSD analysis was applied to calculate bone surface roughness at three relevant size scales: the size scale of cells and large SZ rings in the range of tens of μm ; the size scale of small SZ rings (several μm); and the size scale of podosomes ($1 \mu\text{m}$ or less). The results of the PSD analysis are shown in electronic supplementary material, figure S1. In general, the roughness differences between bone surfaces narrow as the measurement length decreases toward the size of a single podosome.

3.2. Effect of bone topography on sealing zone actin ring size

Differentiated osteoclasts were simultaneously replated on either rough or smooth bone surfaces. Following 24 h incubation, the cells were fixed and stained for actin and nuclei. Examination of the cells showed significant differences in the size of SZ rings developed on the two topographies (figure 2). On the rough surfaces, large rings (with diameters more than $14 \mu\text{m}$) were predominant, constituting 47% of all rings, while small rings (with typical diameters of less than $7 \mu\text{m}$) constitute only 22% of the total ring population (1061 SZ rings counted). On the smooth bone surface an opposite trend was observed: small rings were the predominant phenotype, constituting 53% of total ring population whereas the large rings constituted only 14% (1268 SZ rings counted).

3.3. Effect of bone topography on the sealing zone actin ring dynamics

The observed effect of surface topography on SZ size can be attributed to differences in either ring growth or ring stability. In order to distinguish between these two possibilities, we used time-lapse fluorescence microscopy to track osteoclasts

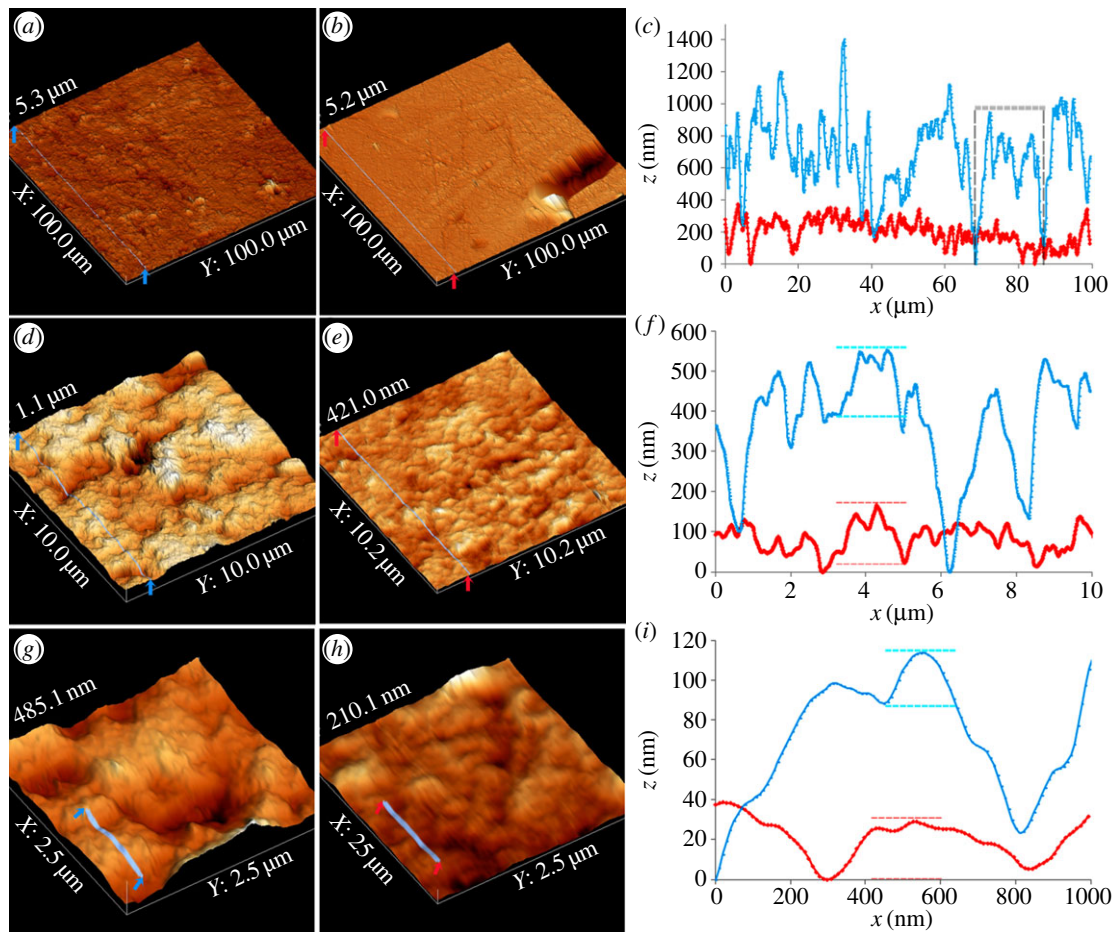


Figure 1. AFM characterization of bone surfaces with different topographies. Three-dimensional representations of rough (left) and smooth (middle) bone surfaces at different scan sizes, with the corresponding height profiles (right). The line profiles (blue, rough surface; and red, smooth surface) were taken along the blue lines delimited by arrows in the respective topographic images. (a,b) Three-dimensional representations of 100 μm scans on rough and smooth bone surfaces, respectively. (c) Corresponding line profiles. A representative periodic ridge (boxed area) on the rough surface has lateral dimensions of about 20 μm and heights of about 1 μm , whereas on the smooth surface the height differences are about 200 nm. (d,e) Three-dimensional representations of 10 μm scan on rough and smooth bone surfaces, respectively. At this scale, the smooth bone surface seems ‘coarsened’, as the smaller surface protrusions become visible. (f) Corresponding line profiles; the smaller protrusions composing the ridges on rough surface (blue line) have lateral dimensions of 1–2 μm and height of about 200 nm, comparable to the topography of smooth surface (red line). (g,h) Magnification of 2.5 μm area from the 10 μm scan demonstrates the similarities between surface topographies at this scale. (i) Line profiles: each protrusion is approximately 200 nm wide and 40 nm high both on the rough and on the smooth surface.

stably expressing GFP-actin for a period of about 20 h. Ring lifetime was calculated as the number of frames (imaged at 1 min intervals) in which the ring remained intact. Similar to the observations in fixed cells, live osteoclasts showed size variations of the developed SZ rings, yet the predominance of smaller rings on the smooth surface and larger rings on the rough surfaces was retained. Two representative cells, growing on rough and smooth surfaces, are shown in figure 3, demonstrating the changes in ring size over time. Typically, cells display an initial period when dynamic SZ rings, which disintegrate while still small, are the most prevalent. This is followed by a period of ring growth, which persisted for several hours, until SZ ring retraction and collapse.

In order to determine the basis for the observed differences in SZ size and dynamics on the different surfaces, we monitored the lifetimes and the local stability of the dynamic SZs which did not grow, and the growing SZs on each of the topographies. Lifetime measurements were carried out manually for individual rings and the imaging of local stability was based on temporal ratio movies (see §2.4), in which pixels depicting stable actin intensities are coloured yellow

and increased or decreased intensity, coloured red or blue, respectively.

The dynamic, small SZ rings are usually preceded by a focal actin cloud that expands symmetrically to form a small ring (3–7 μm) which remains stable for about 2–3 min. These rings, which fail to grow, display similar local stability (figure 4a,b) and lifetimes (figure 4c) on smooth and rough bone topographies, although the sizes were slightly smaller on the smooth surfaces (figure 4d).

We have also addressed the effect of bone microtopography on actin intensity within individual SZs. For this purpose, we plotted the fluctuations of fluorescence intensity with time along SZ cross sections (electronic supplementary material, figure S2). For all the SZs analysed, the intensity fluctuations are not symmetrical at the two sides of the ring, both on rough and smooth bone topographies (compare electronic supplementary material, figure S2a–c to figure S2d–f).

The short-lived small rings show high initiation rate, making it unclear whether or not their formation is centrally coordinated throughout the cell. To address this issue we performed a cross-correlation analysis [47] measuring the

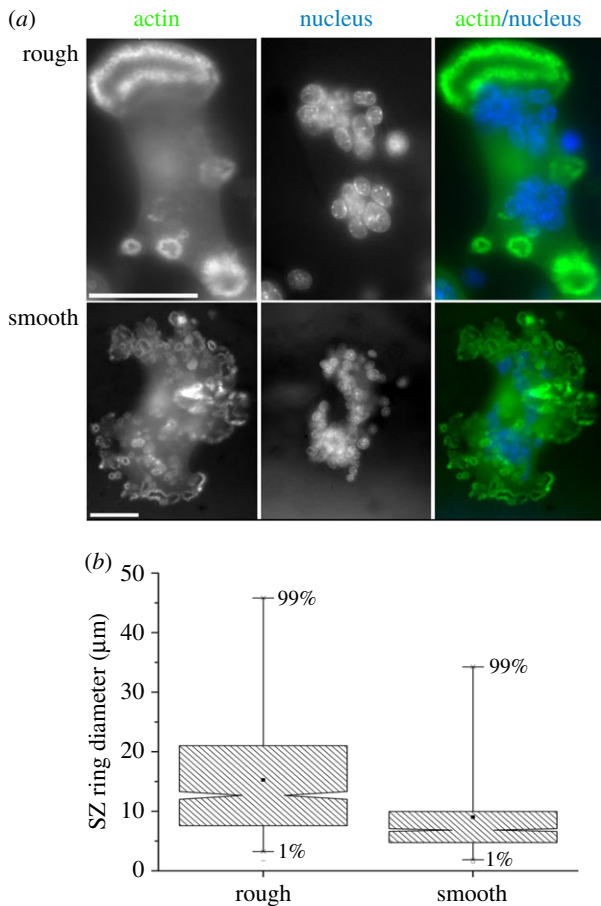


Figure 2. Osteoclasts adhering to different bone topographies differ in the size of their SZ rings. (a) Representative fluorescence images of RAW 264.7 cells plated on rough and smooth bone surfaces and stained for actin (left panels), nuclei (middle panels) and actin and nuclei overlaid (right panels). Scale bars: 50 μm . (b) Box chart of 25–75% of the SZ ring size populations on each of the surfaces. Whiskers show the values of the 1st and 99th percentiles. Black squares inside the box show the median values of each population, and the notch locations show that there is a significant difference between the sizes of the different populations ($p < 0.0001$).

kinetics of ring formation and dissociation throughout the same cell within a period of 60 min. The same procedure was applied to different cells plated on surfaces with the same or with different topographies (electronic supplementary material, figure S3). This analysis indicated that for all the pairs examined (i.e. different rings within the same or nearby cells, on both smooth or rough surfaces; $N = 18$) the calculated correlation coefficient was less than 0.2, indicating that the formation of small rings is locally regulated at the individual SZ level, and is not globally induced.

SZ rings that did not collapse within minutes can grow via expansion, fusion or both. In general, rings grow primarily through continuous expansion, with ring fusion being a secondary process either prior to expansion, or simultaneous to it. Unlike the fast turning rings, expansion to form large rings (figure 5) occurs in a non-uniform manner, through dynamic areas that are distributed along the ring's perimeter (figure 5*a,b*). The observed shift towards larger SZs on the rough bone surfaces is attributed to a longer expansion process (rather than differences in expansion rates), as can be appreciated from the individual kinetic plots (figure 5*a,b*—right) and from the similarity in the average expansion rate (figure 5*c*). The longer lifetimes of expanding SZs observed

on rough surface correlate with higher local stability (more yellow/green pixels in the temporal ratio analysis).

We have also analysed the secondary growth mechanism of SZ rings, ring fusion (figure 6). Fusion occurs when neighbouring rings apparently form contact with each other. This process is usually accompanied by local destabilization in one or both of the rings. This initial stage in ring fusion is reversible, and considerably longer on rough bone than on smooth, resulting in an overall slower fusion process (figure 6*c*). At the next, irreversible stage the contact area shared by the two rings extends and then (usually within minutes) disassembles, resulting in a larger ring that retains the overall combined outline of the parental rings.

4. Discussion

Osteoclasts can sense multiple environmental cues, including chemical cues such as substrate composition and physical cues, and respond to them by altering their development, dynamics and functionality [16,31,48,49]. This environmental sensing capacity is in concert with the growing awareness that adhesive interactions with the extracellular matrix, beyond their morphogenic functions, also integrate multiple external cues and drive a coherent cellular response [50–54]. This consideration assumes even greater importance in the case of resorbing osteoclasts on bone, which require maintenance of tight adhesion to surfaces that not only are heterogeneous in space, but are continuously modified during the progression of resorption. There are thus compelling reasons to test the effects of substrate microtopography on osteoclasts using the natural substrate of these cells, namely bone, rather than uniform synthetic surfaces presenting varied roughness [15,32]. We have used here freshly sectioned and fully hydrated bone, and selected consecutive bone slices for the preparation of paired rough and smooth surfaces. The use of devitalized bone allows observation of the effect of the physical parameter that we wish to study, i.e. microtopography, in the absence of added biological factors, such as osteocyte signalling.

Unlike well characterized features presented by modified artificial surfaces, the composite bone surfaces present a local heterogeneity of chemical and physical features including an intrinsic microtopography profile, irrespective of whether they were polished or not (figure 1). The different scales of roughness on the polished and unpolished surfaces allowed us to relate the effect on SZ structure and dynamics to a range of lateral scales, from a sub- μm scale of the order of a single podosome, up to a scale of tens of micrometres of the order of growing SZs and whole cells (electronic supplementary material, figure S1). In the bone structure, collagen fibrils and carbonate apatite crystals are in the sub- μm size range, the size range of individual podosome components, whereas bone lamellae are in the range of 10 μm and osteons of hundreds of micrometres. It is noteworthy that osteoclasts and their SZs normally do not exceed tens of micrometre sizes when located at their physiological environment (namely bone) while in culture they can reach sizes of hundreds of micrometres [25,55,56]. Herein, both smooth and rough bone surfaces present small topographic features at a characteristic size of few μm with roughness at the sub- μm scale, while only the rough bone presents in addition larger and steeper features. Thus, the differences

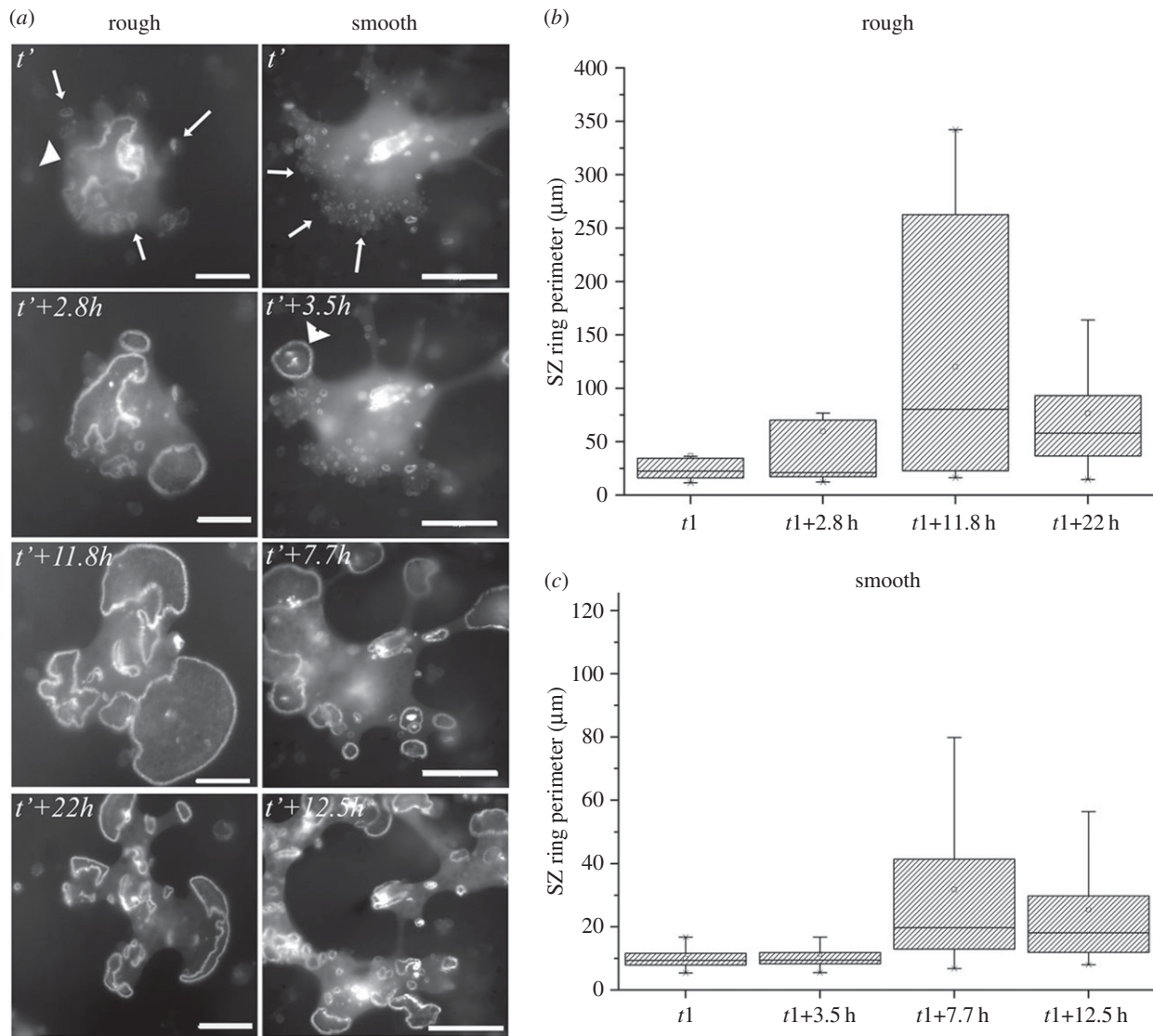


Figure 3. Temporal changes in SZ ring size. (a) Frames from time-lapse movies, showing the changes in average SZ size over time on rough and smooth bone topographies. Time intervals are indicated at the top left corner of each frame. On the rough bone surface (left panels) at the beginning of the movie (t'), a large ring (arrowhead) and multiple small rings (arrows) are observed. Within 3 h, additional rings started to grow. After reaching a maximal size ($t' + 11.8$ h), the rings collapse and small rings are reformed ($t' + 22$ h). Similar cycles of growth and collapse are observed also on the smooth surface (right panels), except that the change in ring size is faster relative to the rough surface, and the collapse occurs when the rings are smaller. Scale bars: 50 μm . (b,c) Box charts quantifying the SZ ring size change over time on the rough and smooth surfaces respectively. The lower and upper values of the charts represent the 25th and the 75th percentiles of the population, respectively. Whiskers show the values of the 1st and 99th percentiles, and the squares inside the box show the median values of each population. This quantification demonstrates the difference in the time scales and the maximal ring sizes.

observed in the osteoclast adhesive response to the varied microtopography can be attributed to roughness differences at a lateral scale of more than 10 μm , which correspond to the bone structural units of lamellae. We infer from these observations that, if osteoclast activity in physiological conditions is indeed influenced by microtopography, the effect is most probably felt at the structural level of bone lamellae.

On homogeneous, artificial surfaces only small, dynamic actin rings are observed on smooth surfaces, whereas large and stable rings are observed on rough surfaces [32]. By contrast, osteoclasts plated on bone form both small and large rings on both topographies, with proportions which are time dependent (figure 3). We therefore infer that, in contrast to artificial surfaces, the adhesive response to topography of bone surfaces is regulated by multiple factors, including chemical and biochemical signals. Contributing to this notion, cycles of ring growth and collapse are observed both on the rough and on the smooth bone surfaces.

Nonetheless, the change in ring size on smooth surfaces is faster, and the collapse occurs when the rings are smaller. In a recent study correlating between SZs and bone surface ultra-structure [38] we observed at the initial stages of adhesion the formation of small SZs around surface features of few μm in width, and approximately 1 μm in height. The SZ rings matched the surface features in size and shape. At more advanced stages of adhesion the large SZs correspond to characteristic resorption pits, indicating that intensive bone degradation requires longer interaction time. This supports the hypothesis that resorption correlates to the larger length scale of bone structure.

The results presented in this paper indicate that bone surface roughness primarily affects ring growth, rather than ring initiation, as the initiator small SZs displayed a short lifetime of several minutes (figure 4), irrespective of surface roughness differences (electronic supplementary material, figure S1). These small SZ rings, with diameter of only few μm ,

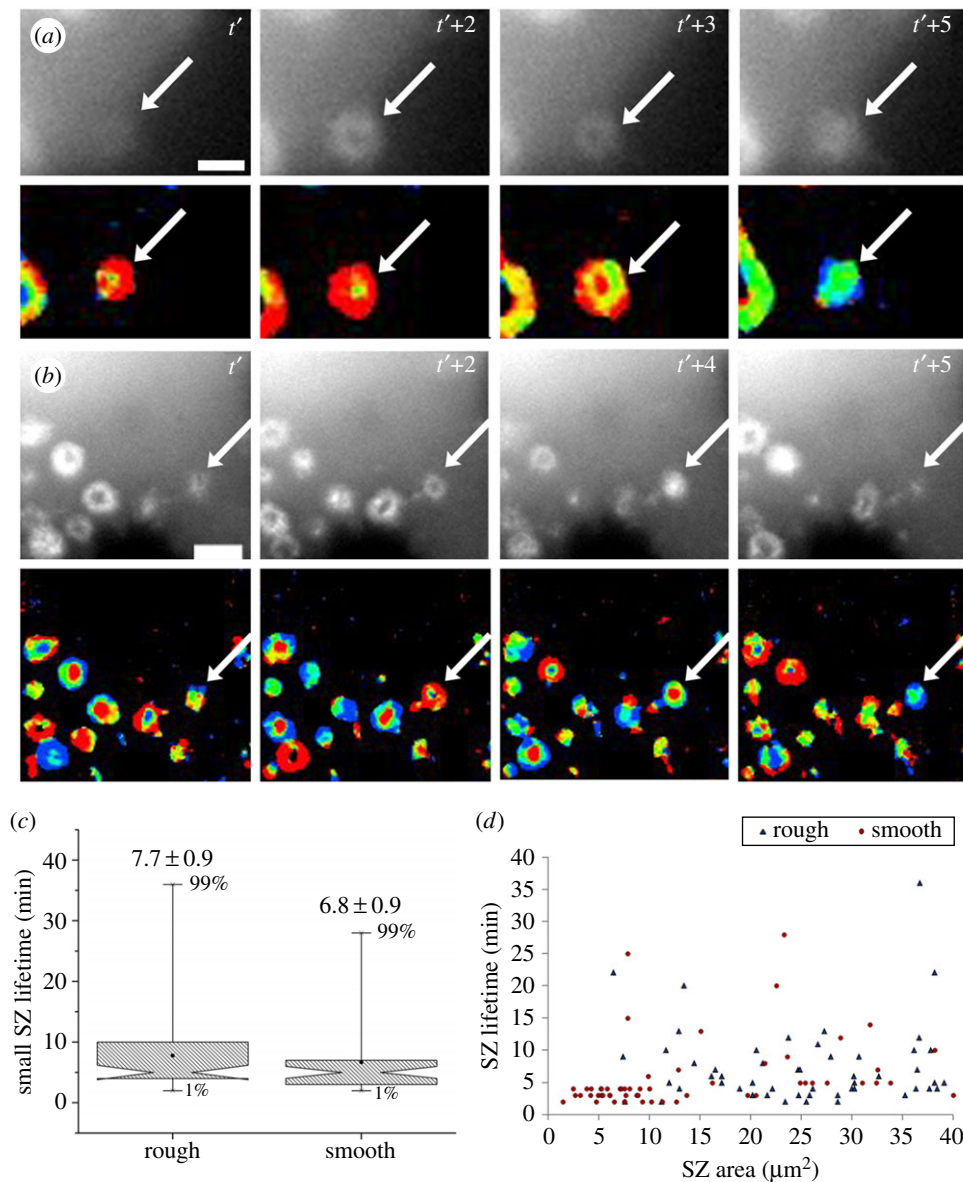


Figure 4. The life cycle of small rings on different bone topographies. (a) Frames from a time-lapse movie of osteoclasts adhering to a rough bone surface (upper panel), and their corresponding temporal ratio frames (lower panel). Local stability is colour-coded: red, newly formed pixels; blue, disappearing pixels, and yellow/green, stable pixels. Time points are noted at the top right of the image. A ring expands out of a pre-formed cloud (arrow). Shortly (5 min) later, the ring collapses. (b) Same as in (a), for cells adhering to the smooth bone surface. Both the time scale and local stability of the cycling rings on the two surfaces are similar. Scale bars: $5 \mu\text{m}$. (c) Box chart of the small ring lifetime distribution. The bottom and top values of the charts represent the 25th and the 75th percentiles of the populations, respectively. Whiskers show the values of the 1st and 99th percentiles. The squares inside the box indicate the median values of each population (also noted above each chart), and the similar locations of the notches demonstrate the statistical similarities between the average values (noted above the boxes). (d) The lifespans of individual small rings as correlated with their sizes. Although on the smooth surfaces the SZ rings are smaller (average area of $14 \mu\text{m}^2$ compared with $25 \mu\text{m}^2$ on rough, $p < 0.001$), this does not seem to affect their lifetime.

behave as a single dynamic unit that either grows radially or collapses. That being said, a closer look at actin intensity, points to asymmetrical temporal variations at different sides of the SZ ring (electronic supplementary material, figure S2), independent of surface topography or overall ring stability. In contrast to observations recently made on macrophages plated on artificial substrates [57], the lack of synchronization in our study can originate from the heterogeneity of the bone surface, which triggers local responses variable within the micrometre range.

What distinguishes growing SZs from those that disassemble at an early stage? It appears that a lifetime of only a few minutes is too short for further growth and stabilization, given that the time periods required for either ring expansion (figure 5) or ring fusion (figure 6), exceed the intrinsic

lifespan of small and dynamic SZs. As a possible trigger for the growth of some SZ rings (either on the smooth surface, or more prominently on the rough bone), we have previously observed the stabilization of small SZ rings by local bone protrusions with matching size [38]. Examination of the growing rings (more than $10 \mu\text{m}$) indicated that unlike the small rings that either grow or uniformly collapse, the growing SZs display non-uniform dynamic behaviour, containing stable and unstable segments. On smooth surfaces this spatial instability is highly prominent, leading to frequent SZ collapse at earlier stages. On rough surfaces, the stable segments play a dominant role in keeping the SZ intact and moderate the effect of the flanking unstable segments, as demonstrated by the longer lifetimes of growing SZs (figures 3 and 5) and the slower fusion (figure 6). This notion is in line with

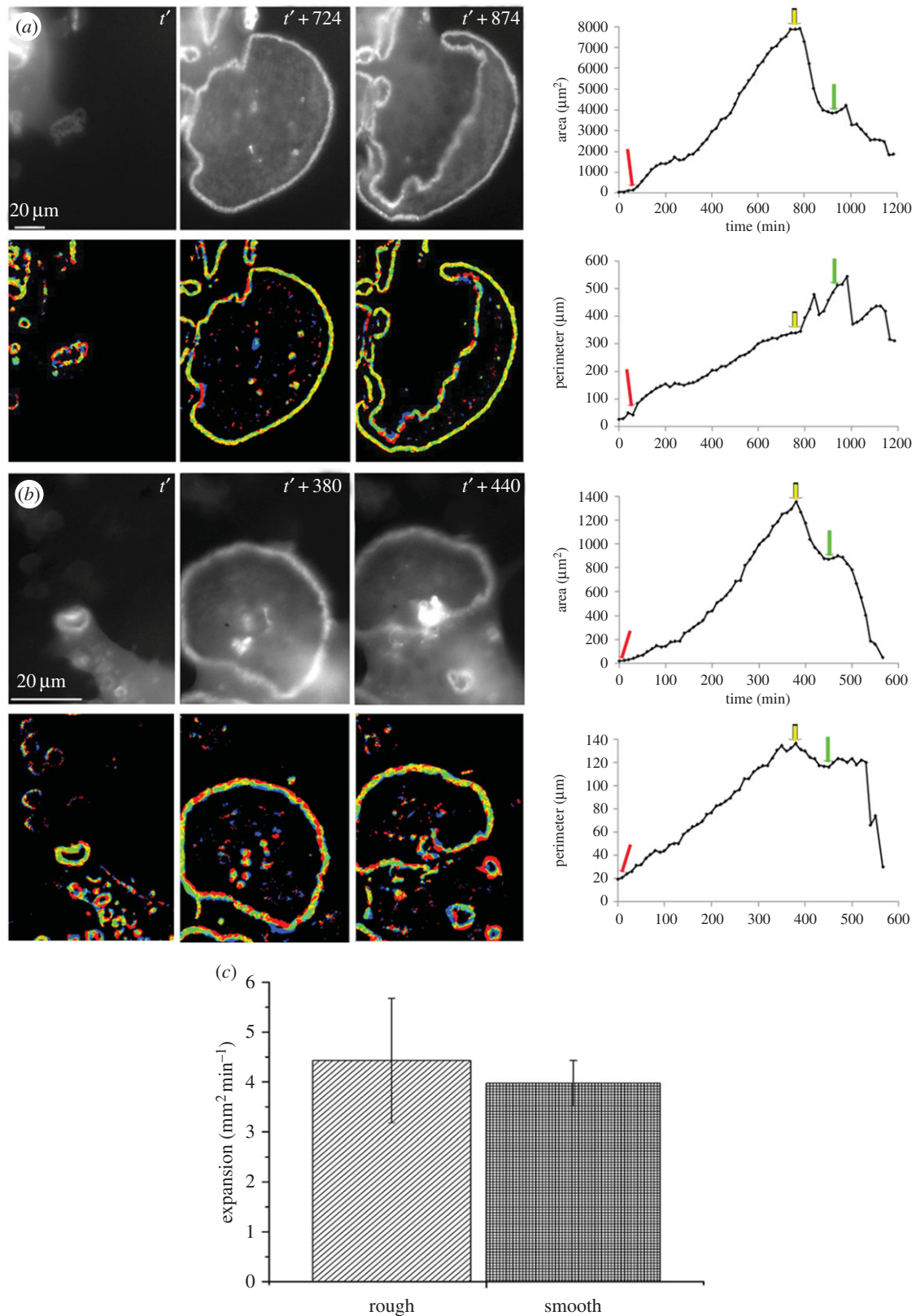


Figure 5. SZ ring growth through expansion. (a) Representative expanding ring on the rough bone surface. Upper panels: frames from fluorescence time-lapse movie. Time points are noted at the top right of the images. Lower panels: frames from corresponding temporal ratio analysis. Ring expansion occurs via dynamic sections of formation (red) and destruction (blue), distributed between stable (yellow/green) sections. After reaching a maximal size ($t' + 724$ min) the ring retracts, its local dynamic instability increases, and ring roundness decreases ($t' + 874$ min). Scale bar: 20 μm . Right side panels: detailed kinetics, showing the change in ring area (above) and perimeter (below) at time intervals of 20 min. Red arrow = time point t' ; yellow arrow = $t' + 724$ min, green arrow = $t' + 874$ min. The area of the retracting ring decreases rapidly, but the perimeter increases due to the deviation from a circular shape. (b) Same as (a) for a representative SZ ring on the smooth bone surface. Note that both the time scale and the maximal SZ size are smaller in (b) relative to (a). (c) Average values ($N = 7$ on each of the surfaces) of the change in ring area per expansion time. Average expansion rate is statistically similar for rings on both surfaces ($3.98 \pm 0.4 \text{ mm}^2 \text{min}^{-1}$ on smooth bone, compared with $4.4 \pm 1.2 \text{ mm}^2 \text{min}^{-1}$ on rough bone).

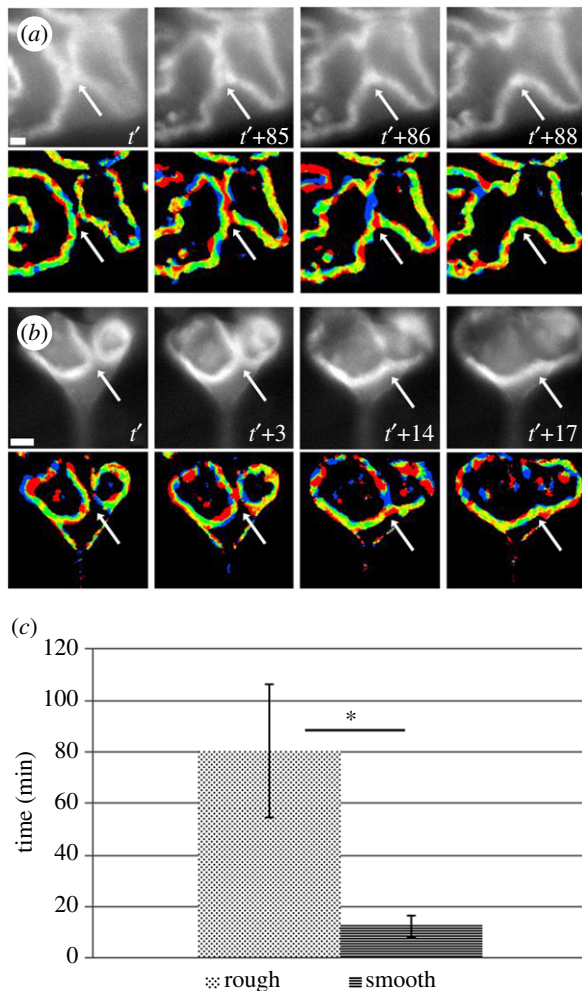


Figure 6. SZ growth through ring fusion. (a) Fusion between rings on rough bone surface. Upper panels: frames from time-lapse fluorescence movie. Time points are noted at the lower right of the image. Lower panels: frames from the corresponding temporal ratio movie, demonstrating the local stability of the rings. Arrow denotes the fusion area. Fusion begins as neighbouring rings form an initial reversible contact (t') that after a certain period of time ($t' + 85$) evolves into a contact area fully shared by both rings. For the fused ring to form, the contact area must first disassemble ($t' + 86$). Finally, a larger ring is formed ($t' + 88$). (b) The same process is observed on smooth bone, but the time scale between first contact (t') and formation of a shared contact area ($t' + 3$) is significantly shorter. (c) Average time scale for fusion of rings on both topographies. Rings on rough bone fuse during a period of 80 ± 25 min on average, compared to 12 ± 4 min on smooth bone ($*p = 0.01$).

previous results demonstrating that an expanding SZ ring can be robust enough to pull itself across significant topographic obstacles [15]. The ability to tolerate local areas of destabilization within a growing SZ reflects the crowded three-dimensional arrangement of podosomes in the larger rings, with their cores connected via the radial and inter-podosome actin fibres [58]. The degree of positive cooperativity between the interconnected podosomes increases as the SZ grows and the number of podosomes increases. Therefore, for a SZ ring to be active in osteoclastic resorption, a sufficient degree of cooperativity is required, via topographic

stabilization or other cues. Such cues can include, for example, the switch associated with the protein SWAP-70, which is required for efficient resorption and which reduced expression results in osteopetrosis [59,60].

The adhesive response to bone is determined by both local and global aspects interweaved. The global response includes the expansion rate of growing SZs (figure 5c), acting at the whole cell level, and the gradual progression in SZ size with time (see figure 3 and electronic supplementary material, movies 1 and 2), in which the initial dynamic phase of small SZs is replaced with a persistent growth phase, which, at some point, is followed by withdrawal and collapse. These cyclic phases are seen in all cells, regardless of surface topography, and the transition between them is often synchronized and coupled with cell migration. The physiological significance of this global regulation process is uncertain at this stage, though it may correspond to cyclic shifts of osteoclasts between resorptive and migratory states [10,61–63].

5. Summary and conclusion

We have studied the dependence of SZ size and stability on bone surface microtopography. We show here that the initiation of SZ ring formation is a largely roughness-independent process. Nevertheless, a local stabilization of growing rings on the rough bone slices enables them to reach considerably larger sizes relative to that obtained on smooth bone slices. This local stabilization potentially translates into resorptive capabilities, as larger and more stable SZs are required for efficient resorption. In the bone ultrastructure the order of magnitude where differences are observed, at the level of tens of micrometres, corresponds to lamellar units, raising the possibility of direct osteoclast sensing of the bone native structure, a direction that we are currently investigating. We suggest that on bone, the adhesive apparatus of osteoclasts is regulated both locally and globally by the chemical and physical properties of the underlying bone, affecting SZ formation and stability.

Authors' contributions. M.S., L.A. and B.G. designed the experiments and analysed the data; M.S. performed the experiments. All authors were involved in writing the paper and had final approval of the submitted version.

Competing interests. We declare we have no competing interests.

Funding. This study was supported by the Jeanne and Joseph Nissim Foundation for Life Sciences Research, Israel Science Foundation (3001/13) and Gerhardt M. J. Schmidt Minerva Center of Supramolecular Architecture.

Acknowledgements. We thank B. Morgenstern for her skilled editing of the manuscript; the laboratory of R. Shahar for their assistance with bone cutting; Y. Halfin and T. Levi from 'Moo & Moo', Rehovot, for supplying fresh cattle femur according to our specifications; A. Livne for his good advice on image analysis and quantification methods. L.A. is the incumbent of the Dorothy and Patrick Gorman Professorial Chair of Biological Ultrastructure; B.G. is the incumbent of the Erwin Neter Professorial Chair in Cell and Tumor Biology.

References

- Weiner S, Traub W. 1992 Bone structure: from angstroms to microns. *FASEB J.* **6**, 879–885.
- Black J, Mattson R, Korostoff E. 1974 Haversian osteons: size, distribution, internal structure, and orientation. *J. Biomed. Mater. Res.* **8**, 299–319. (doi:10.1002/jbm.820080512)

3. Takahashi H, Hattner R, Epker BN, Frost HM. 1964 Evidence that bone resorption precedes formation at the cellular level. *Henry Ford Hosp. Med. Bull.* **12**, 359–364.
4. Frost HM. 1987 Bone ‘mass’ and the ‘mechanostat’: a proposal. *Anat. Rec.* **219**, 1–9. (doi:10.1002/ar.1092190104)
5. Henriksen K, Neutsky-Wulff AV, Bonewald LF, Karsdal MA. 2009 Local communication on and within bone controls bone remodeling. *Bone* **44**, 1026–1033. (doi:10.1016/j.bone.2009.03.671)
6. Xiong J, Onal M, Jilka RL, Weinstein RS, Manolagas SC, O’Brien CA. 2011 Matrix-embedded cells control osteoclast formation. *Nat. Med.* **17**, 1235–1241. (doi:10.1038/nm.2448)
7. Mulcahy LE, Taylor D, Lee TC, Duffy GP. 2011 RANKL and OPG activity is regulated by injury size in networks of osteocyte-like cells. *Bone* **48**, 182–188. (doi:10.1016/j.bone.2010.09.014)
8. Andrews NA. 2012 Osteocyte supply of RANKL meets bone remodeling demand. *IBMS BoneKey* **9**, 212. (doi:10.1038/bonekey.2012.212)
9. Blair HC *et al.* 2009 Osteopetrosis with micro-lacunar resorption because of defective integrin organization. *Lab. Invest.* **89**, 1007–1017. (doi:10.1038/labinvest.2009.58)
10. Saltel F, Destaing O, Bard F, Eichert D, Jurdic P. 2004 Apatite-mediated actin dynamics in resorbing osteoclasts. *Mol. Biol. Cell* **15**, 5231–5241. (doi:10.1091/mbc.E04-06-0522)
11. Nakamura I, Takahashi N, Sasaki T, Jimi E, Kurokawa T, Suda T. 1996 Chemical and physical properties of the extracellular matrix are required for the actin ring formation in osteoclasts. *J. Bone Miner. Res.* **11**, 1873–1879. (doi:10.1002/jbmr.5650111207)
12. Shimizu H, Sakamoto S, Sakamoto M, Lee DD. 1989 The effect of substrate composition and condition on resorption by isolated osteoclasts. *J. Bone Miner. Res.* **6**, 261–275. (doi:10.1016/0169-6009(89)90033-0)
13. Anderegg F, Geblinger D, Horvath P, Charnley M, Textor M, Addadi L, Geiger B. 2011 Substrate adhesion regulates sealing zone architecture and dynamics in cultured osteoclasts. *PLoS ONE* **6**, e28583. (doi:10.1371/journal.pone.0028583)
14. Nakamura I *et al.* 1999 Role of alpha(v)beta(3) integrin in osteoclast migration and formation of the sealing zone. *J. Cell Sci.* **112**, 3985–3993.
15. Geblinger D, Zink C, Spencer ND, Addadi L, Geiger B. 2012 Effects of surface microtopography on the assembly of the osteoclast resorption apparatus. *J. R. Soc. Interface* **9**, 1599–1608. (doi:10.1098/rsif.2011.0659)
16. Marchisio M, Di Carmine M, Pagone R, Piattelli A, Miscia S. 2005 Implant surface roughness influences osteoclast proliferation and differentiation. *J. Biomed. Mater. Res. Part B Appl. Biomater.* **75**, 251–256. (doi:10.1002/jbm.b.30287)
17. Linder S, Aepfelbacher M. 2003 Podosomes: adhesion hot-spots of invasive cells. *Trends Cell Biol.* **13**, 376–385. (doi:10.1016/S0962-8924(03)00128-4)
18. Destaing O, Saltel F, Géminard J-C, Jurdic P, Bard F. 2003 Podosomes display actin turnover and dynamic self-organization in osteoclasts expressing actin-green fluorescent protein. *Mol. Biol. Cell* **14**, 407–416. (doi:10.1091/mbc.E02-07-0389)
19. Saltel F, Chabadel A, Bonnefey E, Jurdic P. 2008 Actin cytoskeletal organisation in osteoclasts: a model to decipher transmigration and matrix degradation. *Eur. J. Cell Biol.* **87**, 459–468. (doi:10.1016/j.ejcb.2008.01.001)
20. Pfaff M, Jurdic P. 2001 Podosomes in osteoclast-like cells structural analysis and cooperative roles of paxillin, proline-rich tyrosine kinase 2 (Pyk2) and integrin α V β 3. *J. Cell Sci.* **114**, 2775–2786.
21. Helfrich M *et al.* 1996 β 1 integrins and osteoclast function: involvement in collagen recognition and bone resorption. *Bone* **19**, 317–328. (doi:10.1016/S8756-3282(96)00223-2)
22. van den Dries K *et al.* 2013 Dual-color superresolution microscopy reveals nanoscale organization of mechanosensory podosomes. *Mol. Biol. Cell* **24**, 2112–2123. (doi:10.1091/mbc.E12-12-0856)
23. Linder S, Kopp P. 2005 Podosomes at a glance. *J. Cell Sci.* **118**, 2079–2082. (doi:10.1242/jcs.02390)
24. Luxenburg C, Addadi L, Geiger B. 2006 The molecular dynamics of osteoclast adhesions. *Eur. J. Cell Biol.* **85**, 203–211. (doi:10.1016/j.ejcb.2005.11.002)
25. Geblinger D, Geiger B, Addadi L. 2009 Surface-induced regulation of podosome organization and dynamics in cultured osteoclasts. *Chembiochem* **10**, 158–165. (doi:10.1002/cbic.200800549)
26. Jiang X, Takayama S, Qian X, Ostuni E, Wu H, Bowden N, LeDuc P, Ingber DE, Whitesides GM 2002 Controlling mammalian cell spreading and cytoskeletal arrangement with conveniently fabricated continuous wavy features on poly(dimethylsiloxane). *Langmuir* **18**, 3273–3280. (doi:10.1021/la011668+)
27. Clark P, Connolly P, Curtis A, Dow J, Wilkinson C. 1987 Topographical control of cell behaviour. I. Simple step cues. *Development* **99**, 439–448.
28. Berry CC, Campbell G, Spadicino A, Robertson M, Curtis AS. 2004 The influence of microscale topography on fibroblast attachment and motility. *Biomaterials* **25**, 5781–5788. (doi:10.1016/j.biomaterials.2004.01.029)
29. Oakley C, Brunette D. 1993 The sequence of alignment of microtubules, focal contacts and actin filaments in fibroblasts spreading on smooth and grooved titanium substrata. *J. Cell Sci.* **106**, 343–354.
30. Choi S, Coonrod S, Estroff L, Fischbach C. 2015 Chemical and physical properties of carbonated hydroxyapatite affect breast cancer cell behavior. *Acta Biomater.* **24**, 333–342. (doi:10.1016/j.actbio.2015.06.001)
31. Webster TJ, Ergun C, Doremus RH, Siegel RW, Bizios R. 2001 Enhanced osteoclast-like cell functions on nanophase ceramics. *Biomaterials* **22**, 1327–1333. (doi:10.1016/S0142-9612(00)00285-4)
32. Geblinger D, Addadi L, Geiger B. 2010 Nanotopography sensing by osteoclasts. *J. Cell Sci.* **123**, 1503–1510. (doi:10.1242/jcs.060954)
33. Duplat D *et al.* 2007 The *in vitro* osteoclastic degradation of nacre. *Biomaterials* **28**, 2155–2162. (doi:10.1016/j.biomaterials.2007.01.015)
34. Vashishth D, Behiri J, Bonfield W. 1997 Crack growth resistance in cortical bone: concept of microcrack toughening. *J. Biomech.* **30**, 763–769. (doi:10.1016/S0021-9290(97)00029-8)
35. Verborgt O, Gibson GJ, Schaffler MB. 2000 Loss of osteocyte integrity in association with microdamage and bone remodeling after fatigue *in vivo*. *J. Bone Miner. Res.* **15**, 60–67. (doi:10.1359/jbmr.2000.15.1.60)
36. Vashishth D, Tanner K, Bonfield W. 2000 Contribution, development and morphology of microcracking in cortical bone during crack propagation. *J. Biomech.* **33**, 1169–1174. (doi:10.1016/S0021-9290(00)00010-5)
37. Grizon F, Aguado E, Huré G, Baslé M, Chappard D. 2002 Enhanced bone integration of implants with increased surface roughness: a long term study in the sheep. *J. Dent.* **30**, 195–203. (doi:10.1016/S0300-5712(02)00018-0)
38. Shemesh M, Addadi S, Milstein Y, Geiger B, Addadi L. 2016 Study of osteoclast adhesion to cortical bone surfaces: a correlative microscopy approach for concomitant imaging of cellular dynamics and surface modifications. *ACS Appl. Mater. Interfaces* **8**, 14932–14943. (doi:10.1021/acsami.5b08126)
39. Martínez JFG, Nieto-Carvajal I, Abad J, Colchero J. 2012 Nanoscale measurement of the power spectral density of surface roughness: how to solve a difficult experimental challenge. *Nanoscale Res. Lett.* **7**, 174. (doi:10.1186/1556-276X-7-174)
40. Kiely JD, Bonnell DA. 1997 Quantification of topographic structure by scanning probe microscopy. *J. Vac. Sci. Technol. B* **15**, 1483–1493. (doi:10.1116/1.589480)
41. Horcas I, Fernández R, Gómez-Rodríguez JM, Colchero J, Gómez-Herrero J, Baro AM. 2007 WSXM: a software for scanning probe microscopy and a tool for nanotechnology. *Rev. Sci. Instrum.* **78**, 13705–13708. (doi:10.1063/1.2432410)
42. Schröder S, Duparré A, Coriand L, Tünnermann A, Penalver DH, Harvey JE. 2011 Modeling of light scattering in different regimes of surface roughness. *Opt. Express* **19**, 9820–9835. (doi:10.1364/OE.19.009820)
43. Zamir E, Katz B-Z, Aota S-I, Yamada KM, Geiger B, Kam Z. 1999 Molecular diversity of cell-matrix adhesions. *J. Cell Sci.* **112**, 1655–1669.
44. Schindelin J *et al.* 2012 Fiji: an open-source platform for biological-image analysis. *Nat. Methods* **9**, 676–682. (doi:10.1038/nmeth.2019)
45. Wessa P. 2012 Free statistics software, Office for Research Development and Education, version 1.1. 23-r7. <http://www.wessa.net>.
46. Utku FS, Klein E, Saybasili H, Yucesoy CA, Weiner S. 2008 Probing the role of water in lamellar bone by dehydration in the environmental scanning electron microscope. *J. Struct. Biol.* **162**, 361–367. (doi:10.1016/j.jsb.2008.01.004)
47. Li L, Caldwell GE. 1999 Coefficient of cross correlation and the time domain correspondence.

- J. Electromyogr. Kinesiol.* **9**, 385–389. (doi:10.1016/S1050-6411(99)00012-7)
48. Park J, Bauer S, Schlegel KA, Neukam FW, von der Mark K, Schmuki P. 2009 TiO₂ nanotube surfaces: 15 nm—an optimal length scale of surface topography for cell adhesion and differentiation. *Small* **5**, 666–671. (doi:10.1002/sml.200801476)
 49. Redey S, Razzouk S, Rey C, Bernache-Assollant D, Leroy G, Nardin M, Cournot G. 1999 Osteoclast adhesion and activity on synthetic hydroxyapatite, carbonated hydroxyapatite, and natural calcium carbonate: relationship to surface energies. *J. Biomed. Mater. Res.* **45**, 140–147. (doi:10.1002/(SICI)1097-4636(199905))
 50. Boudreau N, Bissell MJ. 1998 Extracellular matrix signaling: integration of form and function in normal and malignant cells. *Curr. Opin. Cell Biol.* **10**, 640–646. (doi:10.1016/S0955-0674(98)80040-9)
 51. Geiger B, Bershadsky A, Pankov R, Yamada KM. 2001 Transmembrane crosstalk between the extracellular matrix and the cytoskeleton. *Nat. Rev. Mol. Cell Biol.* **2**, 793–805. (doi:10.1038/35099066)
 52. Geiger B, Bershadsky A. 2002 Exploring the neighborhood: adhesion-coupled cell mechanosensors. *Cell* **110**, 139–142. (doi:10.1016/S0092-8674(02)00831-0)
 53. Schwarz US, Erdmann T, Bischofs IB. 2006 Focal adhesions as mechanosensors: the two-spring model. *Biosystems* **83**, 225–232. (doi:10.1016/j.biosystems.2005.05.019)
 54. Parsons JT, Horwitz AR, Schwartz MA. 2010 Cell adhesion: integrating cytoskeletal dynamics and cellular tension. *Nat. Rev. Mol. Cell Biol.* **11**, 633–643. (doi:10.1038/nrm2957)
 55. Szewczyk KA, Fuller K, Chambers TJ. 2013 Distinctive subdomains in the resorbing surface of osteoclasts. *PLoS ONE* **8**, e60285. (doi:10.1371/journal.pone.0060285)
 56. Kasahara T, Imai S, Kojima H, Katagi M, Kimura H, Chan L, Matsusue Y. 2010 Malfunction of bone marrow-derived osteoclasts and the delay of bone fracture healing in diabetic mice. *Bone* **47**, 617–625. (doi:10.1016/j.bone.2010.06.014)
 57. Proag A, Bouissou A, Mangeat T, Voituriez RL, Delobelle P, Thibault C, Vieu C, Maridonneau-Parini I, Poincloux R. 2015 Working together: spatial synchrony in the force and actin dynamics of podosome first neighbors. *ACS Nano* **9**, 3800–3813. (doi:10.1021/nn506745r)
 58. Luxenburg C, Geblinger D, Klein E, Anderson K, Hanein D, Geiger B, Addadi L, Cordes N. 2007 The architecture of the adhesive apparatus of cultured osteoclasts: from podosome formation to sealing zone assembly. *PLoS ONE* **2**, e179. (doi:10.1371/journal.pone.0000179)
 59. Garbe AI *et al.* 2012 Regulation of bone mass and osteoclast function depend on the F-actin modulator SWAP-70. *J. Bone Miner. Res.* **27**, 2085–2096. (doi:10.1002/jbmr.1670)
 60. Roscher A, Hasegawa T, Dohnke S, Ocaña-Morgner C, Amizuka N, Jessberger R, Garbe AI. 2016 The F-actin modulator SWAP-70 controls podosome patterning in osteoclasts. *Bone Rep.* **5**, 214–221. (doi:10.1016/j.bonr.2016.07.002)
 61. Deguchi T, Alanne MH, Fazeli E, Fagerlund KM, Pennanen P, Lehenkari P, Hänninen PE, Peltonen J, Näreoja T. 2016 *In vitro* model of bone to facilitate measurement of adhesion forces and super-resolution imaging of osteoclasts. *Sci. Rep.* **6**, 22585. (doi:10.1038/srep22585)
 62. Rumpel M, Würger T, Roschger P, Zwettler E, Sturmlechner I, Altmann P, Fratzl P, Rogers MJ, Klaushofer K. 2013 Osteoclasts on bone and dentin *in vitro*: mechanism of trail formation and comparison of resorption behavior. *Calcif. Tissue Int.* **93**, 526–539. (doi:10.1007/s00223-013-9786-7)
 63. Kikuta J *et al.* 2013 Dynamic visualization of RANKL and Th17-mediated osteoclast function. *J. Clin. Invest.* **123**, 866–873. (doi:10.1172/jci65054)